Journal of Materials Chemistry C

Accepted Manuscript

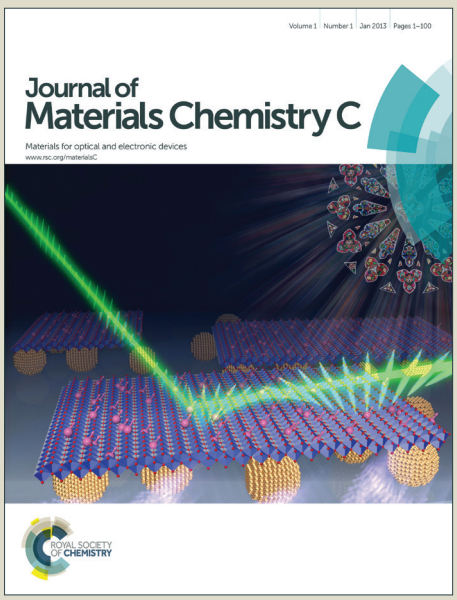

ROYAL SOCIETY OF CHEMISTRY

www.rsc.org/materialsC

Journal of Materials Chemistry C

RSCPublishing

ARTICLE

Graphene/Carbonyl Iron Cross-Linked Composites with Excellent Electromagnetic Wave Absorption Properties

Cite this: DOI: 10.1039/x0xx00000x

Received 00th January 2012,
Accepted 00th January 2012

DOI: 10.1039/x0xx00000x

www.rsc.org/

Zetao Zhu[a], Xin Sun[b], Hairong Xue[a], Hu Guo[a], Xiaoli Fan[a], Xuchen Pan[a], Jianping He[a, *]

Graphene is a highly desirable material for efficient electromagnetic wave absorption as its strong dielectric loss and low density. However, the main drawbacks in pristine graphene such as high dielectric constant and low permeability, inevitably limit its performance due to the poor impedance matching. In this paper, reduced graphene oxide-spherical carbonyl iron composites (RGO-SCI) have been successfully fabricated through a facile wet chemical method. As expected, the apparent improvement of the standard of impedance matching in electromagnetic wave absorption could be found through the combination of RGO and SCI. A carbon bridge effect was adopted to explain the electromagnetic wave absorbing process which is closely related to a cross-linked framework structure of as-synthesized composites. Besides, in the range of 7.79-11.98 GHz with the thickness of 3.0 mm, the RGO-SCI composites exhibited efficient electromagnetic wave absorption characteristics (RL<10 dB) with the minimum reflection loss of -52.46 dB.

Introduction

Electromagnetic wave absorbing material, a kind of functional composites, which could be used for degradation of electromagnetic energy effectively by converting it into heat or other forms of energy.[1] Recently, considerable attention has been paid to the design and development of highly efficient EM absorbing materials due to the increasing demand for civil, commercial and military in the gigahertz (GHz) band range.[2, 3] Consequently, absorbing materials in particular for wide operating frequency band, strong absorption ability, low density, high thermal stability and superior anti-oxidative ability are in high demand.[4-6]

Graphene, a two-dimensional (2D) honeycomb lattice structure, which is composed of carbon six-membered rings, is the foundation of the structure of allotrope of fullerenes, carbon-nanotubes and graphite.[7, 8] Its unique physical and chemical properties make it potential in many applications, such as fuel cells,[9] lithium ion batteries,[10] biotechnology,[11] supercapacitors,[12] liquid crystal devices,[13] photocatalysis[14] and the electromagnetic wave absorbing material,[15-18] etc. Various methods have been proposed and investigated to synthesize graphene, including chemical vapor deposition (CVD),[19] liquid-phase exfoliation,[20] the epitaxial growth[21] and chemical reduction of graphene oxide,[22] etc. The graphene materials synthesized by chemical method are limited in many applications due to the defects and oxygen-containing functional groups,[23] but it might be a potential candidate for absorbing material. The surface defects and functional groups on RGO produced through chemical reduction of graphene oxide may effectively improve the ability of penetration and absorption of electromagnetic waves. Not only could RGO increase the impedance matching characteristics and promote the continuous state to the Fermi energy level transition, but also introduce the polarization relaxation caused by defects and polar functional groups.[24] However, the other two vital factors determining the electromagnetic wave absorption performance, i.e. impedance matching and attenuation characteristic, should not be neglected as well.[25, 26] Obviously, pristine RGO could not meet the demands of ideal electromagnetic wave absorbing materials. Firstly, pristine RGO has high electrical conductivity, which can produce skin effect when the electromagnetic wave incidences, thus affecting its absorbing properties. Secondly, the high permittivity and low permeability of pristine RGO lead to the poor impedance matching. Thereby, the excellent electromagnetic wave absorption performance might not be expected in pristine graphene.

A growing number of electromagnetic wave absorption researches have been reported in various graphene-based composite materials. The strong dielectric loss of composites shows excellent absorbing properties and great utilization potentiality. Chen et al. have successfully prepared high dispersion of uniform sized hexagonal close-packed accumulation of nickel nanocrystals and fcc Ni nano-flowers grown on graphene nanosheets through a mild one-step liquid

phase method. Their study showed the Ni/graphene nanoparticles exhibited superior electromagnetic wave absorption properties to Nickel nanostructures.[27] One of our previous works revealed the enhanced electromagnetic wave absorption performance of RGO after combining with Fe_3O_4 nanoparticles, by utilizing the electric and magnetic loss material complementary effect.[28] SCI have been widely used in the field of electromagnetic wave absorption due to their high Curie temperature, superior thermal stability, high saturation magnetization and magnetic permeability.[29-31] In the current study, a novel strategy to fabricate cross-linked RGO-SCI composites was proposed. We bring forward the concept of RGO combined with micron magnetic particles to improve the electromagnetic loss as well as impedance matching level of composites. As expected, the drastic improvement of impedance matching in electromagnetic wave absorption was found through the combination of SCI on the surface of RGO. A carbon bridge effect was adopted to explain the electromagnetic wave absorbing process which is closely related to the cross-linked framework structure of as-synthesized composites. In addition, the density of as-prepared composites was greatly reduced due to the partial replacement of SCI by low-density carbon-based material of graphene, making it applicable in electromagnetic wave absorption.

Experimental section

Sample preparation

Graphite oxide (GO) was prepared according to the modified Hummers method.[22] RGO-SCI composites were synthesized through a series of liquid phase reaction schemes at room temperature with the following procedures. The surface grafted SCI by aminopropyltrimethoxysilane (APS) was prepared at first. SCI (2.0 g) was suspended into isopropyl alcohol (50 mL) containing APS (1 mL). After ultrasonic treatment for 0.5 h, ammonia solution (0.5 mL) and deionized water (3 mL) were subsequently added to the above-mentioned solvent. After one more hour's ultrasonic treatment, the solvent was removed by magnetic separation and the solid product was washed three times with ethanol. Thereupon, the APS-modified SCI was obtained after drying at 45 ^oC in vacuum. Secondly, the GO dispersion with known concentration was prepared by dispersing a certain quality of GO into 100 mL deionized water under ultrasound irradiation. Thirdly, the as-prepared GO dispersion and APS-modified SCI were simultaneously induced into diluted hydrochloric acid solution (202 mL, 0.336 wt%), followed by mechanical stirring at room temperature for 1 h. The desired solid product was obtained after separation, washed with ethanol and finally dried in a vacuum oven at 45 ^oC for 6 h. GO is reduced by SCI which can be regard as Fe. According to the mass ratio of GO to SCI for 1:5, 3:20, 1:10, and 1:20, the RGO-SCI composites were denoted as RGO-SCI (1), RGO-SCI (2), RGO-SCI (3) and RGO-SCI (4), respectively. The result of Energy-dispersive X-ray spectroscopy (EDS) measurement of RGO-SCI (4) shows the presence of Fe, C and Si in Fig.S3 (In Supplementary Information). A Silicon content of 0.02 wt% can be neglected which was incorporated from APS.

Characterization

The composition and phase purity of the as-synthesized samples were analyzed by Powder X-ray diffraction (XRD, Bruker D8 ADVANCE) with a Cu Kα source (λ=0.154056 nm). The XRD date was recorded from 10^o to 90^o (2θ) with a scanning step of 0.02^o. The Raman spectra were measured by a Jobin Yvon HR 800 confocal Raman system with 632.8 nm diode laser excitation on a 300 lines mm^{-1} grating at room temperature. The surface morphologies were investigated by using a FEI QUANTA 200 scanning electron microscope (SEM). Morphologies, sizes, and distributions of the samples were observed with a transmission electron microscope (TEM, 200 kV, FEI Tecnai G^2). Samples for analysis were prepared by ultrasonically suspending in ethanol and supported on a holey carbon film on a Cu grid. Thermogravimetric (TG) measurements of the products were monitored using a NETZSCH STA 409 PC from 30 to 750 °C under air with a heating rate of 10 °C min^{-1}. FTIR spectra of the samples were determined by FTIR spectrophotometer using a Nicolet NEXUS-670 and KBr pellets of solid samples. The magnetism measurement was performed by a vibrating sample magnetometer (VSM, Quantum Design, PPMS-9). The samples applied for electromagnetic measurements were prepared by homogeneously mixing the hybrid materials with wax (the weight ratio of the prepared powder was around 60%), and then the mixture was pressed into a toroid with an outer diameter of 7.0 mm, inner diameter of 3.04 mm and height of about 3.0 mm. The complex relative dielectric permittivity and magnetic permeability were obtained by measuring the S11 and S21 parameters over 0.5-18 GHz using a vector network analyzer (Agilent N5244A).

Results and discussion

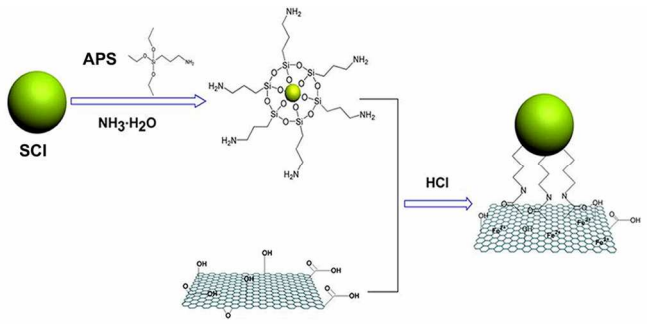

Fig.1. Schematic illustration for the preparation process of RGO-SCI composites.

The schematic diagram of the formation of RGO-SCI composites is illustrated in Fig.1. SCI solid could not be well dispersed in solvent as the striking different polarity between particles and solvent. APS (a common alkyl coupling agent) is a class of functional groups with two different functions in the current synthesis scheme. It is worth noticing that APS adsorbed on the surface of SCI could react with some polar

functional groups as well. FTIR spectra of SCI and APS modified SCI is measured and shown in Fig.S2. The characteristic peaks of APS modified SCI at 1056 and 794 (552) cm^{-1} assigned as Si-O-Si and SiO-H bending vibration, indicating that APS was successfully grafted onto the surface of SCI.[32] The silicon-oxygen bond in APS will be anchored at the surface of SCI, while the positive charged amino groups on the other side could be well bonded with the negative charged oxygen containing functional groups (such as carboxyl groups and hydroxyl groups) on the surface of GO through electrostatic force.[32, 33] Moreover, the Fe^{2+} cations produced from the corrosion of SCI in the present of tiny amount of hydrochloric acid, might be adsorbed onto the surface of SCI particles. GO sheet with negative charges are adsorbed onto the surface of positive charged SCI, thereby strengthen the bonding between GO and SCI. The process of GO reduced by SCI is shown as follows. The tight connection of GO and SCI could promote the efficient charge transfer from the Fe/Fe^{2+} to GO sheets, thus boosting to reduction reactions.
The reduction reaction may be shown as follows,[34]

$$GO + aH^+ + be^- \rightarrow reduced \quad GO + cH_2O$$

Therefore, the reduction of GO and the process of composite formation happened simultaneously by the one-step wet chemical method.

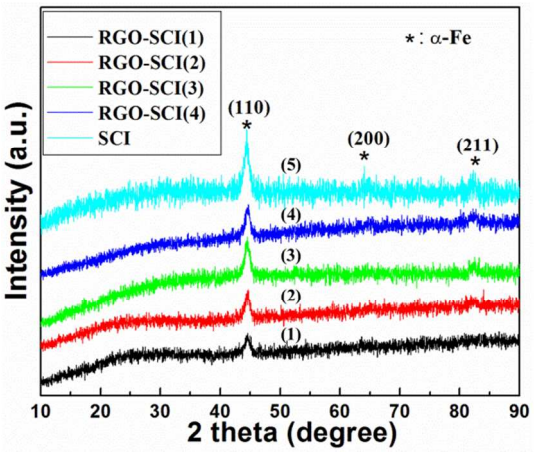

Fig.2. XRD patterns of SCI and RGO-SCI composites.

To investigate the crystal structure and morphology of the products, RGO-SCI composites were characterized by means of powder XRD, Raman spectra detection and SEM. Fig.2 shows the XRD patterns of SCI and RGO-SCI composites with different combination ratios. The diffraction peaks of the SCI are perfectly indexed to the body-centered cubic phase of Fe (JCPDS card 87-0721) and three peaks at 2θ=44.7º / 82.5º / 65º correspond to (110) / (211) / (200) planes of α-Fe, respectively. Two diffraction peaks at 2θ=44.7º / 82.5º are found in the four composites. The peak at 2θ=65º was disappeared due to the covering of RGO networks. Furthermore, it is obviously observed that the intensity of diffraction peaks of the composites are weakened compared with the pure SCI, which is also owing to the cover of RGO.[35] Moreover, compared with Fig.2 (3, 4, 5), Fig.2 (1, 2) show a weak and broad peak at around 23.5º, which is a typical pattern of amorphous carbon structure, indicating that the GO was reduced and the ordered stacking of part of the graphene was destructed with the rising of SCI combination ratio.[27, 36]

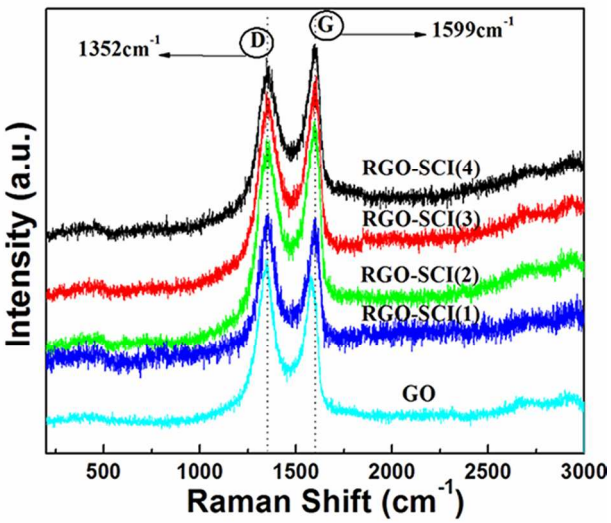

Fig.3. Raman spectra of GO and RGO-SCI composites.

Further structural characterization for the evolution of carbon framework during the reduction process from GO to RGO was reviewed by Raman spectra detection. Raman spectra of SCI and H-SCI (SCI treated by APS and HCl) are shown in Fig.S5. The surface of pristine SCI is oxidized to the mixture of α-Fe_3O_4 and α-Fe_2O_3. And α-Fe_3O_4 is oxidized to α-Fe_2O_3 on the surface of H-SCI.[37] Here, it could be seen when adding SCI in the composite, the peaks corresponding to SCI disappear due to the covering of RGO networks. As depicted in Fig.3, the as-prepared RGO-SCI composites exhibit two strong signals centered at 1352 and 1599 cm^{-1}, which correspond to the D and G bands of carbonaceous species, respectively. The D band at 1352 cm^{-1} is assigned to the vibrations of sp^3 carbon atoms of disordered graphite and the G band at 1599 cm^{-1} is related to the in-plane vibration of sp^2 carbon atoms in a 2D hexagonal lattice.[38-40] The intensity ratio of the D and G band (I_D/I_G) is a useful indicator to evaluate the size of sp^2 domains and structural disorder of graphene nanosheets.[41,42] The I_D/I_G ratios of GO, RGO-SCI (1), RGO-SCI (2), RGO-SCI (3) and RGO-SCI (4) are calculated at 1.203, 1.028, 0.9534, 0.929 and 0.891, respectively. The highest I_D/I_G for GO can be found clearly as the plenty of oxidation groups in GO synthesized by Hummer's method. Plus, it can be found that the I_D/I_G declined with increasing mass ratio of SCI and RGO, indicating the decrease of oxidation groups in RGO. The reason might be caused by the much thinner and more uniform RGO coating layers on SCI formed under higher SCI amount participated in the preparation, which could promote the reduction progress of RGO dramatically.

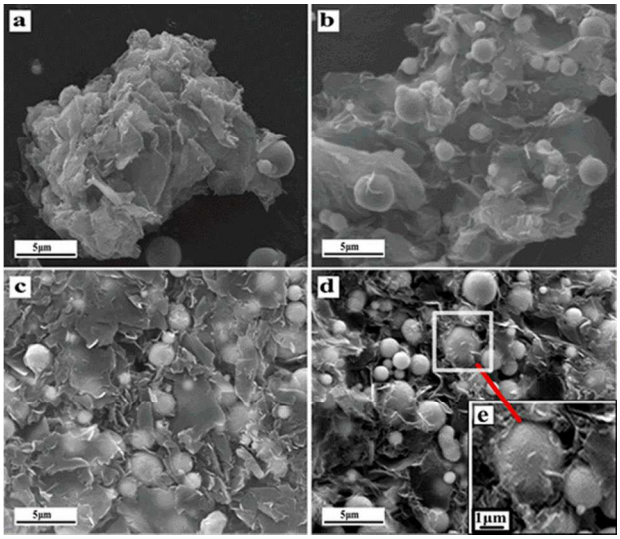

Fig.4. SEM images of (a) RGO-SCI (1), (b) RGO-SCI (2), (c) RGO-SCI (3) and (d) RGO-SCI (4). The inset of Fig.4 (d) shows the SEM image of RGO-SCI (4) with high magnification (e).

To further understand the morphology of as-prepared composites, SEM measurements were carried out. Fig.4 shows the SEM images of composites with different SCI combination ratios. As shown in Fig.4 (a), it can be seen that a large amount of RGO aggregate into a big block of structured carbon, and only a small number of SCI particles are scattered filling into the space of RGO block when a tiny amount of SCI is combined with RGO. For the composites with the higher combination ratio of SCI, as shown in Fig.4 (b) and (c), the SCI is found to be tightly inserted into the RGO sheets, which supports and isolates RGO sheets effectively. More pore space existed in successive RGO networks could be filled by SCI if further increasing the combination ratio of SCI to RGO (As shown in Fig. 4(d, e)). Moreover, it is worth noticing that the RGO sheets tend to be thinner and a few SCI particles are scattered uniformly at the edge of RGO. With the SCI combination ratio rising, the thickness of RGO progressively becomes smaller, meanwhile the SCI disperses more uniformly, reflecting the supporting role of SCI skeleton.

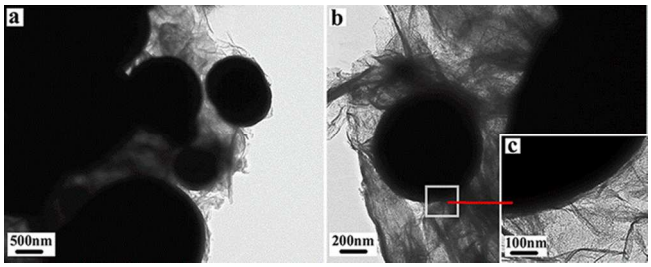

Fig.5. TEM images of RGO-SCI (2) composite with different magnifications.

Furthermore, the TEM images of RGO-SCI (2) are used to characterize the morphological deeply. As shown in Fig.5, the thin RGO sheets of composite have a crumpled and rippled structure. The SCI powders with a nonuniform size of around 1-3 μm are anchored onto the thin graphene sheets. SCI particles of around 1 μm and interface between RGO and SCI could be observed. Obviously, SCI powders and RGO sheets show a typical cross-linked framework structure while SCI powders are wrapped by RGO networks and RGO networks are separated by SCI. SCI powders act as the framework to support the RGO, which will prevent RGO sheets from restacking. RGO sheets act as the network to separate SCI, which could prevent SCI from agglomerating and enable a good dispersion of SCI particles over the RGO.

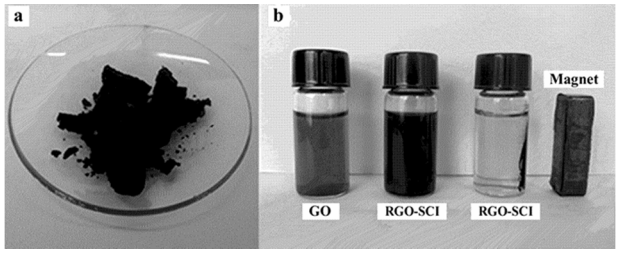

Fig.6. (a) photographs of RGO-SCI (1) composite and (b) RGO-SCI (1) aqueous dispersion after ultrasonic treatment.

As shown in Fig.6 (b), graphite oxide (GO) could be well dispersed in aqueous solution as its hydrophilic property caused by the abundant hydrophilic organic groups in GO. Golden yellow and red could be respectively observed at low and high concentration, suggesting that the concentration of GO in aqueous solution influences the optical absorption. After combination with SCI, however, the dispersion turns turbid and the suspended solids are black shown in Fig.6, which is attributed to the generation of hydrophobic RGO. The black suspended solids could be easily attracted from solution under an external magnetic field generated by placing a magnet near the vial, indicating the well combination between RGO and SCI which is prerequisite for the further reduction of GO to RGO.

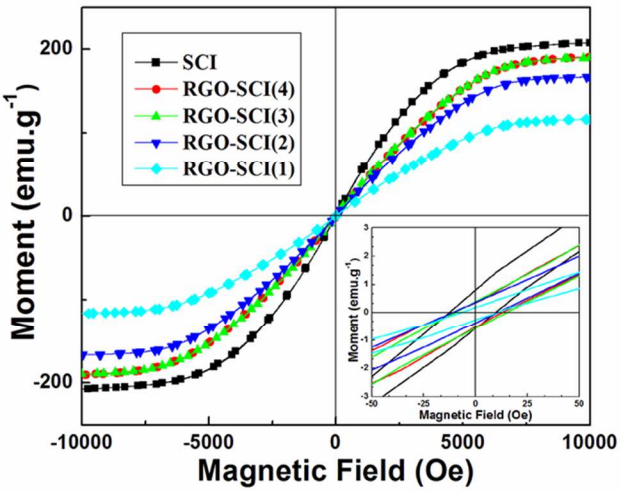

Fig.7. Room-temperature magnetic hysteresis loops of SCI and as-prepared RGO-SCI composites; the inset figure shows the enlarged low-field hysteresis loops.

Tab.1. Magnetic properties of RGO-SCI composites

Sample	Ms/emu g^{-1}	Hc/Oe	Mr/emu g^{-1}
RGO-SCI (1)	116.5	7.5	0.3
RGO-SCI (2)	169.9	10.5	0.5
RGO-SCI (3)	188.7	13.5	0.7
RGO-SCI (4)	190.7	13.5	0.7
SCI	207.7	13.8	0.8

Ms: saturation magnetization; Hc: coercivity; Mr: remnant magnetization.

It is well known that the magnetic properties of small size material are influenced by structure and shape anisotropy. Fig.7 shows the hysteresis loops of SCI and RGO-SCI measured at room temperature, including Ms, Mr and Hc. The magnetic parameters corresponding to Fig.7 are also shown in Tab.1. As we know, carbonyl iron is a typical soft magnetic material with high Ms and low Hc. As depicted in Fig.7, the RGO-SCI composites exhibit large Ms, and Ms increasing with the rising of SCI combination ratio. The Hc of RGO-SCI composites experience a slight increase trend with the increase of SCI combination ratio, which should be attributed to the much thinner non-magnetic isolating layer produced from RGO as well as the weakened interaction force between the SCI. But the really small Hc makes the increase trend less obvious. In addition, the small area inside magnetic hysteresis loop suggests the small minority of magnetic hysteresis loss in the magnetic loss.

For an efficient electromagnetic wave absorbing material, there are three key factors to be satisfied, i.e. low density, strong absorption property and wide absorption frequency range. In the current investigation, we combine RGO with SCI to build a cross-linked framework structure where RGO sheets were cross-linked for the construction of RGO networks and SCI confined in the network acted as framework to support RGO network can be seen in TEM images (Fig.5).[33] There are four main advantages of this design. Firstly, such design could considerably reduce the density of composites due to the partial replacement of SCI by much lighter RGO, which would be promising in practical applications. Secondly, the cross-linked structure proposed in this work could inhibit the aggregation of magnetic particles and provide large contact area. Thirdly, the optimal impedance matching characteristic could be achieved easily by adjusting the electromagnetic parameters in as-proposed composites which integrate the dielectric material (RGO) and magnetic material (SCI) with controllable combination ratio. Finally, the proposed composite structure where magnetic particles are linked with RGO provides a great electron transfer channel between SCI particles, leading to the formation of conductive network and the drastic electronic polarization. Therefore the efficient electromagnetic wave absorbing property could be achieved through carbon bridge effect. The electromagnetic parameters and electromagnetic wave absorption properties of the as-prepared samples discussed in the follows will further prove this effect.

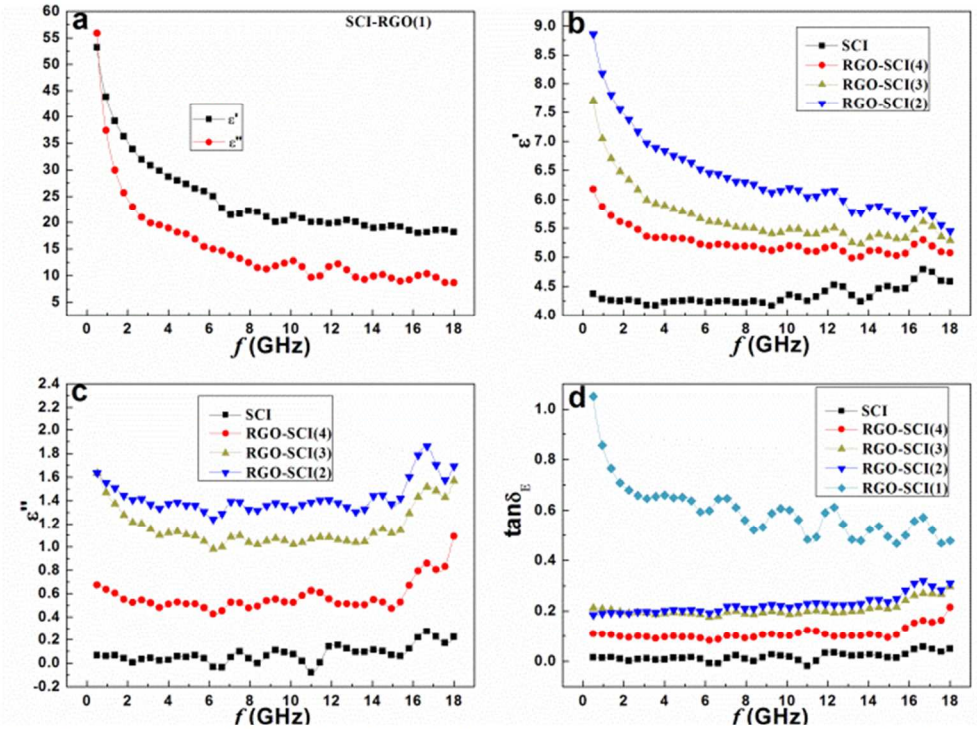

Fig.8. Frequency dependence of (a) permittivity of RGO-SCI (1) and (b) real and (c) imaginary parts of complex permittivity of RGO-SCI (2), RGO-SCI (3), RGO-SCI (4) and SCI, and dielectric loss tangents of samples.

The absorbing properties of materials can be estimated from their dielectric and magnetic properties. The complex permittivity and dielectric loss tangent as a function of frequency are shown in Fig.8 (a-d). The electromagnetic

parameters versus frequency in the range of 0.5-18 GHz of RGO-SCI composites and SCI were measured and shown in Fig.8 (a-c). Generally, the loss tangent (tanδ) is applied to characterize the loss properties of the incident electromagnetic wave in an absorber. The dielectric loss tangent $\tan\delta_E$ ($\tan\delta_E = \varepsilon''/\varepsilon'$) is calculated based on the measured complex permittivity of the composites and shown in Fig.8 (d). It can be seen that the real part ε′ of SCI keeps constant around 4.3 in the range of 2-9 GHz, and then increases slightly and several wave peaks emerges at 9-18 GHz. Meanwhile, both ε″ and $\tan\delta_E$ almost keep zero in the whole frequency band, indicating the weak dielectric loss of pristine SCI. As is shown in Fig.8 (a, d), ε′, ε″ and $\tan\delta_E$ become a very high value after the combination with a small amount of SCI, indicating a strong dielectric loss in RGO-SCI (1). According to the free electron theory: $\varepsilon'' \approx 1/2\pi\varepsilon_0\rho f$, where ε_0 is the permittivity of a vacuum, ρ is the resistivity, f is the frequency of the electromagnetic wave.[43] Obviously, the strong dielectric loss of graphene caused by the high value of ε″ comes from its low resistivity derive from the formation of the large conducting network. Therefore, the strong dielectric loss of RGO-SCI (1) is attributed to the high combination ratio of RGO and SCI. However, the excellent electromagnetic wave absorption properties result from the efficient complementarity between the appropriate permittivity and permeability in materials. No matter whether it is high magnetic loss or the high dielectric loss may induce a poor electromagnetic wave absorption property due to the unbalance impedance match.[44] As shown in Fig.8 (a), the excessive complex permittivity of RGO-SCI (1) decreases the degree of impedance matching and leads to poor electromagnetic wave absorption property. From Fig.8 (b-d), ε′ value of RGO-SCI (2), RGO-SCI (3), RGO-SCI (4) dramatic decreases with increasing frequency from 8.9, 7.7, 6.2 to 5.6, 5.5, 5.1 in 0.5-18 GHz range, respectively. The ε″ value obviously decreases with increasing frequency from 1.65, 1.63, 0.68 to 1.28, 0.99, 0.49 in the 0.5-6 GHz range, then tend to a stable constant and exhibits a strong peak in the 15-18 GHz range, indicating an obvious frequency scattering. In addition, ε′ and ε″ gradually decrease with the increasing mass ratio of SCI and RGO for the reason that SCI is dispersed into RGO and separate RGO sheets as an isolation material. Obviously, $\tan\delta_E$ decreases with the increasing combination ratio of SCI, illustrating that the addition of SCI can decrease the dielectric loss ability of the composites. Moreover, the defects and functional groups remaining in RGO are apt to accumulate electronic and give rise to electronic polarization, which also causes the emergence of several wave peaks. Thus, we need a suitable combination ratio of RGO and SCI to adjust electromagnetic parameters, which helps improve the level of impedance matching.

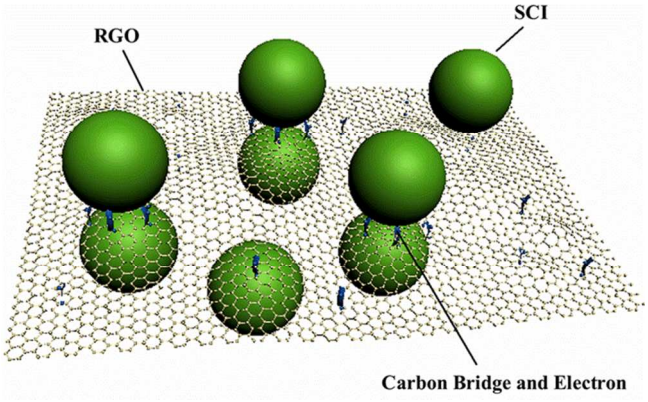

Fig.9. Schematic illustration of electromagnetic wave absorption mechanism through carbon bridge effect in the RGO-SCI composites.

As is shown in Fig.9 with schematic illustration, the cross-linked framework structure also provides a mechanism to strengthen the dielectric loss ability. In the structure of RGO-SCI composites, the construction of a 3D, compactly interconnected graphene network can offer a huge increase in the electrical conductivity.[45] Due to its excellent electrical conduction, RGO behaves as an electron transfer medium agrees well with the bridged structure, where electrons are rapidly transported along the RGO bridges between SCI.[46] The transport of electrons leads to dramatic electron polarization and space charge polarization will increase permittivity, which will improve impedance matching characteristic and enhance dielectric loss ability, making the best of the contribution to electromagnetic wave absorbing property. Therefore, the mechanism to enhance the electromagnetic wave absorbing property could be defined as carbon bridge effect. Therefore, carbon bridge effect has effectively enhanced the dielectric loss ability and electromagnetic wave absorbing property.

Journal of Materials Chemistry C RSCPublishing

ARTICLE

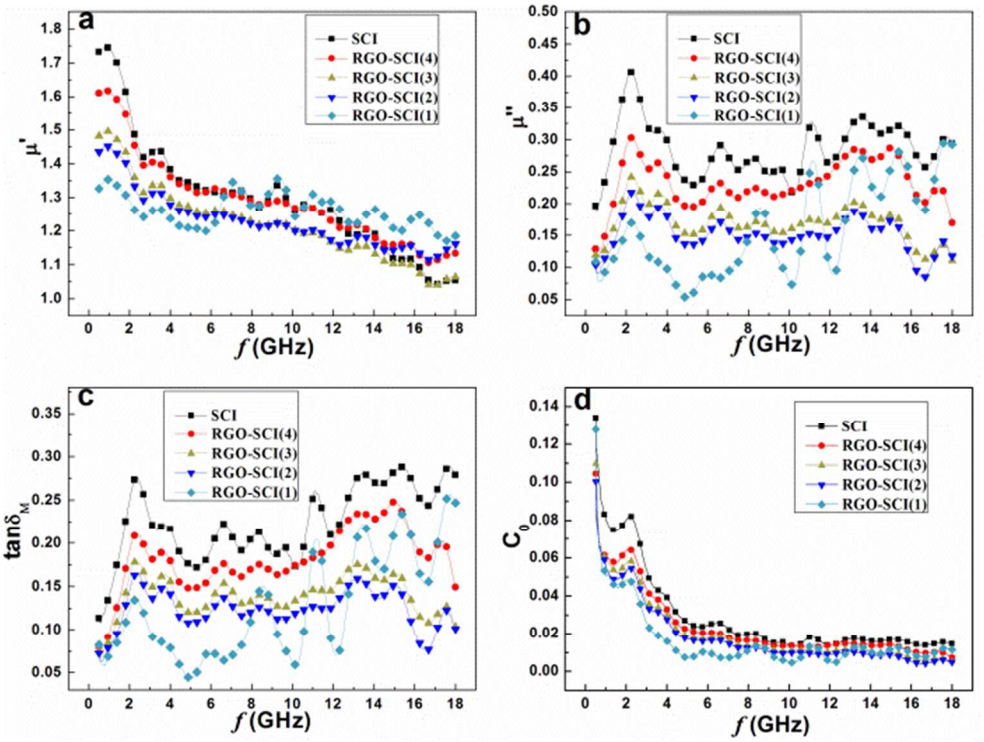

Fig.10. Frequency dependence of (a) real and (b) imaginary parts of complex permeability, the corresponding (c) magnetic loss tangents and (d) C_0-f curves of RGO-SCI and SCI composites.

Fig.10 shows the real part (μ′), imaginary part (μ″) of the complex permeability, magnetic loss tangent and C_0-f curves of RGO-SCI and SCI composites. On one hand, μ′ of RGO-SCI (2), RGO-SCI (3), RGO-SCI (4) and SCI decreases obviously in the range of 0.5-1.8 GHz. It drops from 1.45, 1.5, 1.63, 1.75 to 1.15, 1.05, 1.15, 1.05, respectively. The μ′, μ″ and tanδ increase with the SCI combination ratio rising, as a result of the filling of SCI with strong magnetic in the space of RGO sheets. However, the variation tendency of μ′, μ″ and tanδ of RGO-SCI (1) decrease at first, and then increase which was caused by the structural inhomogeneity owing to the agglomeration of RGO. On the other hand, several resonance peaks appear in μ′ and μ″ in the whole range and the origin was analysed as follows. First, magnetic hysteresis loss whose resonance frequency corresponds to MHz frequency band is not the main magnetic loss mechanism. Second, natural resonance and domain wall resonance may be the main reasons to emerge the resonance peaks. Third, the peaks can also be suggested as eddy current effect when the composites are highly conductive. The loss caused by the eddy current effect can be expressed by C_0, which can be described as $C_0 = \mu''(\mu')^{-2} f^{-1} = 2\pi\mu_0\sigma d$, where σ is conductivity, d is the depth of particle and μ_0 is the vacuum permeability.[47] If C_0 is a constant with the change of frequency, we can say that the magnetic loss is determined by eddy current effect. As Fig.10 (d) shows, C_0 decreases with the increasing frequency in the 0.5-5 GHz range, illustrating that the loss is caused by natural resonance and domain wall resonance instead of eddy current effect. Meanwhile, C_0 keeps a constant in the range of 5-18 GHz, indicating that eddy current effect is the main loss mechanism in this range. Furthermore, the coupled permittivity and permeability also lead to the emergence of multiple peaks.

To reveal the electromagnetic wave absorption performance of as-synthesized RGO-SCI composites, the reflection loss (RL) values of RGO-SCI were calculated using the relative complex permeability and permittivity at a given thickness layer according to transmit line theory, which is backed by a perfect conductor for single absorb layer was calculated as follows,[48]

$$Z_{in} = Z_0\sqrt{\frac{\mu_r}{\varepsilon_r}}\tanh(j\frac{2\pi ft}{c})\sqrt{\mu_r\varepsilon_r}$$

$$RL = 20\lg\left|\frac{Z_{in} - Z_0}{Z_{in} + Z_0}\right|$$

$$Z_0 = \left(\frac{\mu_0}{\varepsilon_0}\right)^{1/2}$$

where Z_0 is the characteristic impedance of free space (377 Ω), Z_{in} is the input impedance of the absorber, ε_0 and μ_0 are the permittivity and permeability of free space, respectively, $\varepsilon_r=\varepsilon'-j\varepsilon''$ and $\mu_r=\mu'-j\mu''$ are the complex permittivity and permeability of the absorber, respectively, c is the velocity of electromagnetic waves in free space, f is the frequency of the electromagnetic wave and d is the thickness of absorbers. The impedance matching condition is determined by the combinations of six parameters: ε', ε'', μ', μ'', f and d, and the RL values versus frequency can be evaluated at a specified thickness from ε_r and μ_r.

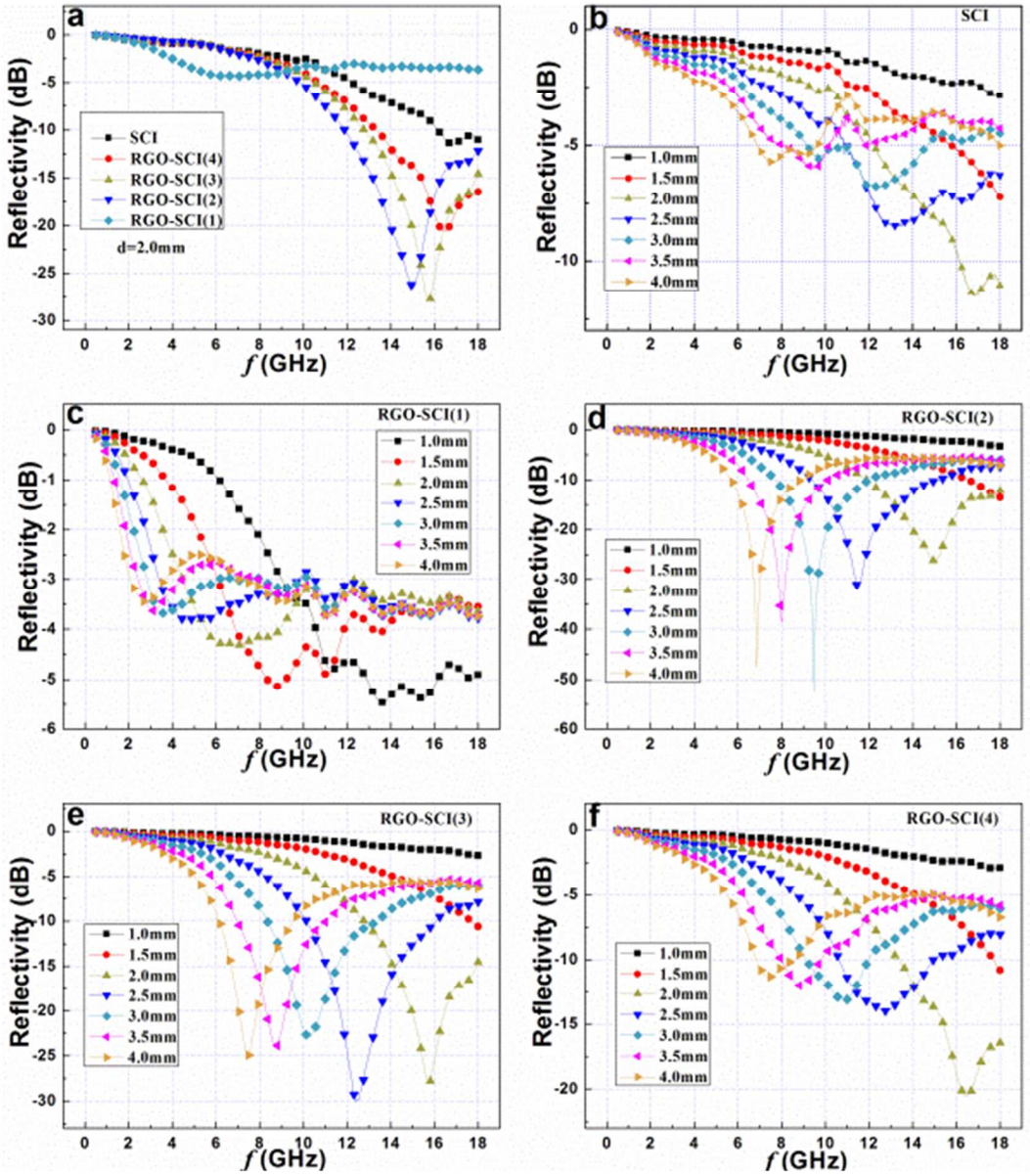

Fig.11. The calculated reflection losses of (a) comparison of electromagnetic wave reflection losses of the five samples with the thickness of 2 mm, (b) SCI, (c) RGO-SCI (1), (d) RGO-SCI (2), (e) RGO-SCI (3) and (f) RGO-SCI (4) paraffin wax composites versus frequency.

Fig.11 (a) shows the calculated RL curves of SCI and RGO-SCI composites with the thickness of 2.0 mm. The RL of SCI is really poor and only a narrow bandwidth under -10 dB at 16-18 GHz. However, the electromagnetic wave absorbing behaviors are greatly improved with the filling of SCI into RGO sheets. The SCI combination amount is critical to the electromagnetic wave absorption property of the hybrid materials. The calculated RL curves of SCI, RGO-SCI (1), RGO-SCI (2), RGO-SCI (3) and RGO-SCI (4) composites with different thicknesses are shown in Fig.11 (b-f). The thickness of the sample is one of the crucial parameters, which affects the intensity and the position of the frequency at the reflection loss minimum. Obviously, the absorption peaks become sharper and transfer to the low frequency with the increase thickness of the

composites, which can be explained by the expression of $f_m = c/(2\pi\mu'' d)$.[49] Meanwhile, as can be seen from Fig.11 (d), the sample of RGO-SCI (2) composite exhibits a strong electromagnetic wave absorption property, and the minimum reflection loss decreases with the increase of sample thickness. There is a strong broad wave absorbing peak centered at 9.46 GHz of SCI-RGO (2) with the thickness of 3 mm, the minimum reflection loss even reaches about -52.46 dB. In the frequency range of 7.79-11.98 GHz, the absorbing area was deeper than -10 dB (means that 90% of the attenuation according to equations that mentioned above) and the wave absorbing area was deeper than -20 dB in the frequency range of 8.89-10.10 GHz. These results show that the RGO-SCI (2) composites with an optimum mass ratio of RGO and SCI possess most efficient electromagnetic wave absorbing activity in both low- and high-frequency bands.

As previously stated, the impedance matching and electromagnetic wave attenuation are two key factors that are contribute to electromagnetic wave absorption performance. In our composites, there are several key factors to adjust electromagnetic parameters, which also have effect on the two factors mentioned above. First, the composites could improve the magnetic loss due to the introduction of the magnetic loss material (SCI) to the electric loss material (RGO), which helps improve the magnetic loss of the composites. And the main magnetic loss mechanisms may be ascribed as natural resonance, domain wall resonance and eddy current effect. Second, RGO networks provide a large contact surface for wrapping on plenty of SCI particles, resulting the decreased conductivity and improved impedance matching performance effectively. Simultaneously, the interfacial polarization and the associated relaxation may be two possible factors, making great contributions to the improved electromagnetic wave absorption properties due to the combination of RGO and SCI. Third, electronic polarization caused by the carbon bridge effect may be another possible loss mechanism. Additionally, the existence of polar functional groups and defects remaining in RGO could increase the dipole polarization in the composites, thus enhancing the dielectric loss ability. We compare RGO-SCI with some similar reported composited in electromagnetic wave absorption properties shown in Tab.2.

Tab.2. Electromagnetic wave absorption parameters of some reported composites and as-prepared RGO-SCI.

Sample	RL_{min} (dB)	Bandwidth (RL<-10dB) (GHz)	f (GHz)	d (mm)	Reference
RGO-Fe_3O_4	-27	4.8-13.6	5.4	2-4	28
Graphene-Ni	-17.5	2.8-4, 11.6-13.5	3.6	5	36
Graphene-polyaniline	-26	7.5-18	8.6	2-4	50
Flake carbonyl iron-Polymer	-39	2.8-8.3	3.3	1-2.5	51
Fe-MWCNTs	-39	1-7.5	2.7	1.8-10	52
Fe-C	-43.1	8.3-12.2, 16.7-18	9.6	1.5-3.1	53
RGO-SCI	-52	5.8-18	9.6	2-4	Our work

Conclusions

In summary, RGO-SCI composites have been successfully synthesized using a one-step wet chemical method. We first time introduce micrometer scale SCI acting as framework to support RGO networks to build a cross-linked framework structure. The proposed uniform RGO-SCI composites could efficiently utilize the benefits from both dielectric RGO and magnetic SCI as well as produce an electromagnetic complementary effect. In addition, a carbon bridge effect is also considered as a reasonable mechanism during the electromagnetic wave absorption process. A strong broad absorbing peak centered at 9.46GHz and the minimum reflection loss even reach -52.46 dB could be achieved on SCI-RGO (2) composite with the thickness of 3.0 mm. In the frequency range of 7.79-11.98 GHz, the absorbing area was deeper than -10 dB and the wave absorbing area was deeper than -20 dB in the frequency range of 8.89-10.10 GHz. We thus believe that the novel composite with both lightweight and high-efficiency absorption property reported herein could stimulate the further development of such functional materials and in-depth understanding of the absorption mechanism.

Acknowledgements

The authors appreciate the financial support from the National Natural Science Foundation of China (51372115).

Notes and references

[a] *College of Materials Science and Technology, Nanjing University of Aeronautics and Astronautics, 210016 Nanjing, PR China.*
[b] *Science and Technology on Electromagnetic Scattering Laboratory, 100854 Beijing, PR China.*
Tel: +86 25 52112900; Fax: +86 25 52112626.
E-mail address: jianph@nuaa.edu.cn

1 C. Tong, Advanced Materials and Design for Electromagnetic Interference, Taylor & Francis, Boca Raton, 2009, 15.

2 S.M. Abbasa, A.K. Dixitb, R. Chatterjeea and T.C. Goel, *Mater. Sci. Eng. B*, 2005, **123**, 167-171.
3 H.L. Zhu, Y.J. Bai, R. Liu, N. Lun, Y.X. Qi, F.D. Han and J.Q. Bi, *J. Mater. Chem.*, 2011, **21**, 13581-13587.
4 Z. Guo, S.E. Leea, H. Kim, S. Parka, H.T. Hahn, A.B. Karki and D.P. Young, *Acta Mater.*, 2009, **57**, 267-277.
5 F.L. Wang, J.R. Liu, J. Kong, Z.J. Zhang, X.Z. Wang, M. Itoh and K.I. Machida, *J. Mater. Chem.*, 2011, **21**, 4314-4320.
6 S.C. Chiu, H.C. Yu and Y.Y. Li, *J. Phys. Chem. C*, 2010, **114**, 1947-1952.
7 J. Liang, Y. Jiao, M. Jaroniec and S.Z. Qiao, *Angew. Chem. Int. Ed.,* 2012, **51**, 11496-11500.
8 S. Stankovich, D.A. Dikin, G.H.B. Dommett, K.M. Kohlhaas, E.J. Zimney, E.A. Stach, R.D. Piner, S.T. Nguyen and R.S. Ruoff, *Nature*, 2006, **442,** 282-286.
9 X. Sun, J.P. He, J. Tang, T. Wang, Y.X. Guo, H.R. Xue, G.X. Li and Y.O. Ma, *J. Mater. Chem.*, 2012, **22**, 10900-10910.
10 W. Li, F. Wang, S.S. Feng, J.X. Wang, Z.K. Sun, B. Li, Y.H. Li, J.P. Yang, A.A. Elzatahry, Y.Y. Xia and D.Y. Zhao, *J. Am. Chem. Soc.*, 2013, **135**, 18300-18303.
11 O. Akhavana, E. Ghaderi, H. Emamy and F. Akhavan, *Carbon*, 2013, **54**, 419-431.
12 E.O. Polat and C. Kocabas, *Nano Lett.*, 2013, **13**, 5851-5857.
13 P. Blake, P.D. Brimicombe, R.R. Nair, T.J. Booth, D. Jiang, F. Schedin, L.A. Ponomarenko, S.V. Morozov, H.F. Gleeson, E.W. Hill, A.K. Geim and K.S. Novoselov, *Nano Lett.*, 2008, **8**, 1704-1708.
14 Y. Dong, Jing Li, L. Shi, J. Xu, X.B. Wang, Z.G. Guo and W.M. Liu, *J. Mater. Chem. A*, 2013, **1**, 644-650.
15 M. Fu, Q.Z. Jiao and Y. Zhao, *J. Mater. Chem. A*, 2013, **1**, 5577-5586.
16 L. Wang, Y. Huang, X. Sun, H.J. Huang, P.B. Liu, M. Zong and Y. Wang, *Nanoscale*, 2014, **6**, 3157-3164.
17 C.G. Hu, Z.Y. Mou, G.W. Lu, N Chen, Z.L. Dong, M.J. Hu and L.T. Qu, *Phys. Chem. Chem. Phys.*, 2013, **15**, 13038-13043.
18 L. Kong, X.W. Yin, Y.J. Zhang, X.Y. Yuan, Q. Li, F. Ye, L.F. Cheng, and L.T. Zhang, *J. Phys. Chem. C,* 2013, **117**, 19701-19711.
19 C. Mattevi, H. Kim and M. Chhowalla, *J. Mater. Chem.*, 2011, **21**, 3324-3334.
20 Y. Hernandez1, V. Nicolosi, M. Lotya, F.M. Blighe, Z.Y. Sun, S. De, I.T. McGovern, B. Holland, M. Byrne, Y.K. Gun'Ko, J.J. Boland, P. Niraj, G. Duesberg, S. Krishnamurthy, R. Goodhue, J. Hutchison, V. Scardaci, A.C. Ferrari and J.N. Coleman, *Nat. Nanotechnol.*, 2008, **3**, 563-568.
21 C. Berger, Z.M. Song, X.B. Li, X.S. Wu, N. Brown, C. Naud, D. Mayou, T.B. Li, J. Hass, A.N. Marchenkov, E.H. Conrad, P.N. First and W.A.D. Heer, *Science*, 2006, **312**, 1191-1196.
22 W. S. Hummers and R. E. Offeman, *J. Am. Chem. Soc.*, 1958, **80**, 1339-1339.
23 N. Ghaderi and M. Peressi, *J. Phys. Chem. C*, 2010, **114**, 21625-21630.
24 C. Wang, X.J. Han, P. Xu, X.L. Zhang, Y.C. Du, S.R. Hu, J.Y. Wang and X.H. Wang, *Appl. Phys. Lett.*, 2011, **98**, 072906.
25 Y.P. Duan, Z. Liu, H. Jing, Y.H. Zhang and S.Q. Li, *J. Mater. Chem.*, 2012, **22**, 18291-18299.
26 G.X. Tong, Q. Hu, W.H. Wu, W. Li, H.S. Qian and Y. Liang, *J. Mater. Chem.*, 2012, **22**, 17494-17504.
27 T.T. Chen, F. Deng, J. Zhu, C.F. Chen, G.B. Sun, S.L. Ma and X.J. Yang, *J. Mater. Chem.*, 2012, **22**, 15190-15197.
28 X. Sun, J.P. He, G.X. Li, J. Tang, T. Wang, Y.X. Guo and H.R. Xue, *J. Mater. Chem. C*, 2013, **1**, 765-777.
29 L.D. Liu, Y.P. Duan, L.X. Ma, S.H. Liu and Z. Yu, *Appl. Surf. Sci.*, 2010, **257**, 842-846.
30 R.B. Yang and W.F. Liang, *J. Appl. Phys.*, 2011, **109**, 07A311.
31 Y. Liu, X.X. Liu and X.J. Wang, *J. Alloys. Compd.*, 2014, **584**, 249-253.
32 S.B. Yang, X.L. Feng, S. Ivanovici and K. Müllen, *Angew. Chem. Int. Ed*., 2010, **49**, 8408-8411.
33 W. Wei, S.B. Yang, H.X. Zhou, I. Lieberwirth, X.L. Feng and K. Müllen, *Adv. Mater.*, 2013, **25**, 2909-2914.
34 Z.J. Fan, W. Kai, J. Yan, T. Wei, L.J. Zhi, J. Feng, Y.M. Ren, L.P. Song and F. Wei, *ACS Nano*, 2010, **5**, 191-198.
35 M. Sathish, T. Tomai, and I. Honma, *J. Power Sources*, 2012, **217**, 85-91.
36 X. Yang, C.L. Chen, J.X. Li, G.X. Zhao, X.M. Ren and X.K. Wang, *RSC Adv.*, 2012, **2**, 8821-8826.
37 D.L.A.D. Faria, S. V. Silva and M.T.D. Oliveira, *J. Raman Spectrosc,* 1997, **28**, 873-878.
38 Z. Jin, J. Yao, C. Kittrell and J.M. Tour, *ACS Nano*, 2011, **5**, 4112-4117.
39 L.Y. Zhao, R. He, K.T. Rim, T. Schiros, K.S. Kim, H. Zhou, C. Gutiérrez, S.P. Chockalingam, C.J. Arguello, L. Pálová, D. Nordlund, M.S. Hybertsen, D.R. Reichman, T.F. Heinz, P. Kim, A. Pinczuk, G.W. Flynn and A.N. Pasupathy, *Science*, 2011, **333**, 999-1003.
40 W.F. Chen, S.R. Li, C.H. Chen and L.F. Yan, *Adv. Mater.*, 2011, **23**, 5679-5683.
41 A.C. Ferrari, J.C. Meyer, V. Scardaci, C. Casiraghi, M. Lazzeri, F. Mauri, S. Piscanec, D. Jiang, K.S. Novoselov, S. Roth and A.K. Geim, *Phys. Rev. Lett.*, 2006, **97**, 187401.
42 F. Tuinstra and J.L. Koenig, *J. Chem. Phys.*, 1970, **53**, 1126.
43 X.F. Zhang, X.L. Dong, H. Huang, Y.Y. Liu, W.N. Wang, X.G. Zhu, B. Lv, J.P. Lei and C.G. Lee, *Appl. Phys. Lett.*, 2006, **89**, 053115.
44 A. Wadhawan, D. Garrett, J. M. Perez, *Appl. Phys. Lett.*, 2003, **83**, 2683.
45 C. Wu, X.Y. Huang, G.L. Wang, L.B. Lv, G. Chen, G.Y. Li and P.K. Jiang, *Adv. Funct. Mater.*, 2013, **23**, 506-513.
46 Z.B. Yang, M.K. Liu, C. Zhang, W.W. Tjiu, T.X. Liu and H.S. Peng, *Angew. Chem. Int. Ed*., 2013, **52**, 3996-3999.
47 X. Gu, W.M. Zhu, C.J. Jia, R. Zhao, W. Schmidt and Y.Q. Wang, *Chem. Commun.*, 2011, **47**, 5337-5339.
48 J.R. Liu, M. Itoh and K. Machida, *Appl. Phys. Lett.*, 2003, **83**, 4017-4019.
49 T. Maeda, S. Sugimoto, T. Kagotani, N. Tezuka and K. Inomata, *J. Magn. Magn. Mater.*, 2004, **281**, 195-205.
50 H.L. Yu, T.S. Wang, B. Wen, M.M. Lu, Z. Xu, C.L. Zhu, Y.J. Chen, X.Y. Xue, C.W. Sun and M.S. Cao, *J. Mater. Chem.*, 2012, **22**, 21679-21685.
51 Z.J. Song, L.J. Deng, J.L. Xie, P.H. Zhou, H.P. Lu and X. Wang, *Surf. Interface Anal.*, 2014, **46**, 77-82.
52 F.S. Wen, F. Zhang and Z.Y. Li, *J. Phys. Chem. C*, 2011, **115**, 14025-14030.
53 X.F. Zhang, X.L. Dong, H. Huang, B. Lv, J.P. Lei and C.J. Choi, *J. Phys. D: Appl. Phys.*, 2007, **40**, 5383-5387.

54 J.N. Zheng, S.S. Li, X.H. Ma, F.Y. Chen, A.J. Wang, J.R. Chen and J.J. Feng, *J. Mater. Chem. A*, 2014, **2**, 8386-8395.
55 G.C. Wang, Z.Y. Yang, X.W. Li and C.Z. Li, *Carbon*, 2005, **43**, 2564-2570.
56 A. Lerf, H.Y. He, M. Forster and J. Klinowski, *J. Phys. Chem. B*., 1998, **102**, 4477-4482.
57 M.A. Aldosari, A.A. Othman and E.H. Alsharaeh, *Molecules*, 2013, **18**, 3152-3167.

TOC

Graphene/Carbonyl Iron Cross-Linked Composites with Excellent Electromagnetic Absorption Properties

Zetao Zhu[a], Xin Sun[b], Hairong Xue[a], Hu Guo[a], Xiaoli Fan[a], Xuchen Pan[a], Jianping He[a] *

[a] College of Materials Science and Technology, Nanjing University of Aeronautics and Astronautics, 210016 Nanjing, PR China

[b] Science and Technology on Electromagnetic Scattering Laboratory, 100854 Beijing, PR China

*Corresponding author. Tel: +86 25 52112900; Fax: +86 25 52112626.

E-mail address: jianph@nuaa.edu.cn (J.P. He)

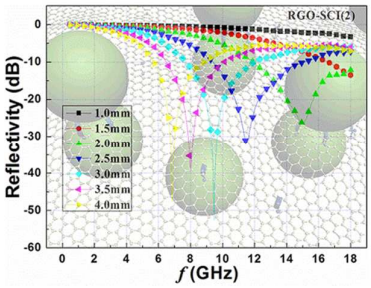

A carbon bridge effect was adopted to explain electromagnetic wave absorbing property related to cross-linked framework structure of RGO-SCI composites.